J. Fluid Mech. (2003), *vol.* 479, *pp.* 327–348.
DOI: 10.1017/S0022112002003695 Printed in the United Kingdom

Cinematographic observation of the collapse and rebound of a laser-produced cavitation bubble near a wall

By OLGERT LINDAU† AND WERNER LAUTERBORN

Drittes Physikalisches Institut, Universität Göttingen, Bürgerstraße 42-44, 37073 Göttingen, Germany

(Received 6 December 2001 and in revised form 4 November 2002)

Collapse and rebound of a cavitation bubble near a wall are revisited with modern experimental means. The bubble is generated by the optical breakdown of the liquid when a strong laser pulse is focused into water. Observations are made with high-speed cinematography; framing rates range between several thousand and 100 million frames per second, and the spatial resolution is in the order of a few micrometres. After formation the bubble grows to a maximum size with a radius of 1.5 mm at the pulse energy used, and in the subsequent collapse a liquid jet evolves on the side opposite the wall and penetrates through the bubble. Using a shadowgraph technique and high framing rates, the emission of shock waves, which is observed at minimum bubble size, is resolved in detail. For a range of stand-off distances between the bubble centre and the wall, a counterjet forms during rebound. The counterjet is clearly resolved to consist of cavitation micro-bubbles, and a quantitative measure of its height evolution is given. Its emergence might be caused by a shock wave, and a possible connection of the observed shock wave scenario with the counterjet formation is discussed. No counterjets are observed when the stand-off distance is less than the maximum bubble radius, and the bubble shape becomes toroidal after the jet hits the wall. The jet impact on the wall produces a pronounced splash, which moves radially outwards in the space between the bubble and the wall. The volume compression at minimum bubble size is found to depend strongly on the stand-off distance. Some of the results are compared to numerical simulations by Tong *et al.* (1999), and the material presented may also be useful for comparison with future numerical work.

1. Introduction

Interest in cavitation bubble dynamics near a wall goes back to the beginning of the last century and was mainly motivated by the urge to understand the destructive action of bubbles on solid surfaces. While the erosion process still remains difficult to resolve in detail, the interest in such bubbles has since broadened. Major experimental contributions to our current view of bubble collapse near a solid wall come from Benjamin & Ellis (1966), Lauterborn & Bolle (1975), and Tomita & Shima (1986), among others. For a brief review and current results on the destructive action of

† Present address: University of California, Department of Mechanical Engineering, Berkeley, CA 94720-1740, USA.

cavitation bubbles on solid surfaces see for example Philipp & Lauterborn (1998) and references therein. Questions of general interest include an understanding of shock waves, luminescence, and the jet and counterjet formation for such transient and non-spherical bubbles.

It has been suggested rather intuitively by Kornfeld & Suvorov (1944) and later on found experimentally by Naudé & Ellis (1961) that during collapse near a solid wall a bubble loses sphericity and develops a liquid jet (a first numerical study of the jet was presented by Plesset & Chapman 1971). The jet forms on the bubble side opposite the solid wall and travels through the bubble. It impacts on the other side of the bubble surface. Even though the role of the jet in the erosion mechanism is controversial, and the damage capability of the jet impact on the wall is now thought to be small, it is clear that the effect of the jet on the bubble dynamics is immense. The processes discussed in this paper, i.e. toroidal bubble collapse, counterjet formation, and to a certain extent also shock wave emission, are directly related to the jet behaviour.

Laser-generated cavitation was developed in the early 1970s and has become a prominent method for experiments with single transient bubbles (see Lauterborn 1972, 1974). Using this method, a strong laser pulse is focused into the bulk of a liquid, and a bubble is generated by optical breakdown. After plasma recombination the bubble expands very reproducibly to an almost perfect sphere, if not disturbed by non-isotropic boundary conditions (or for example created by a highly elongated plasma). An alternative method that has been widely used for the production of transient bubbles is spark generation (see e.g. Benjamin & Ellis 1966 and Tomita & Shima 1986). Spark generation has the drawback that the electrodes that are used for spark creation influence the bubble dynamics. Also, transient bubbles can be generated by a venturi flow (see e.g. Harrison 1952).

Ohl, Lindau & Lauterborn (1998) find that, under certain circumstances, a laser-induced bubble emits light when collapsing near a wall. This luminescence was known from undisturbed, spherical bubbles, and has been reported for example by Buzukov & Teslenko (1971) and Akmanov *et al.* (1974). Light emission from transient cavitation bubbles is now called SCBL (single cavitation bubble luminescence). SCBL intensity strongly depends on the the stand-off distance between bubble centre and wall (see Ohl *et al.* 1999). This is probably due to the compression, which also depends on the stand-off. No light emission could be found in the parameter range that is covered here (i.e. for stand-offs below 4). Recent SCBL studies for undisturbed bubbles include Wolfrum *et al.* (2001), and Baghdassarian *et al.* (2001). Akhatov *et al.* (2001) propose a mathematical model for the spherically symmetric motion of a laser-induced bubble.

In the present study bubble dynamics and shock wave emission of a single laser-generated cavitation bubble are investigated by means of high-speed cinematography. The bubble is produced near a wall and the stand-off distance between the bubble centre at formation and the wall is used to characterize the bubble dynamics. The experimental methods are explained in § 2. Section 3 deals with stand-off distances that are larger than the maximum bubble radius. Using a shadowgraph technique and very high framing rates, a complex shock wave emission scenario is found in the very last stage of bubble collapse. Also, the evolution of the counterjet, a structure that develops in the opposite direction to the jet, is studied quantitatively. In § 4 collapse and rebound are studied for bubbles that are produced closer to the wall. Such bubbles make contact with the wall and create no counterjet.

A first theoretical approach for the pressure developed in a spherical bubble during collapse was presented in the basic work by Rayleigh (1917). The pressure

can be very high and consequently leads to an outgoing shock wave. The first experimental evidence for cavitation noise of a single bubble near a wall is, to our knowledge, given by Harrison (1952) who simultaneously measured bubble dynamics and pressure pulses at a distance from the bubble. In a detailed investigation, Vogel & Lauterborn (1988) observe a very strong dependence of the pressure pulse on the stand-off distance. In more recent studies, it has been found that the pulse resolves into a sequence of shock waves. Such sequences have been made visible, e.g. by Tomita & Shima (1986) and Shaw *et al.* (1996) employing a schlieren technique, and by Ward & Emmony (1991) using interferometry. Ohl, Philipp & Lauterborn (1995) use high-speed cinematography and a shadowgraph illumination for visualization. In the present study the shock wave emission is investigated with a setup similar to that of Ohl *et al.* (1995), but framing rate and spatial resolution are higher than in all previous studies. A very complex propagation scenario is resolved, and an interplay between the bubble dynamics and the shock wave motion is found.

For a certain range of stand-off distances a counterjet forms during rebound. It emerges very fast and grows in the opposite direction to the liquid jet, where it stays visible for a long time. Even though the counterjet can be found in older recordings, for example in the work by Harrison (1952), or Kling & Hammitt (1972), its first description is in Lauterborn (1974). The counterjet is a peculiar entity. Its origin is not known yet with certainty. In fluid dynamic simulations a counterjet does not appear (see e.g. Best 1993; Zhang, Duncan & Chahine 1993; Blake *et al.* 1997, and references therein). However, its appearance is an experimental fact as it can also be found in more recent publications (see e.g. Tomita & Shima 1986; Vogel, Lauterborn & Timm 1989; Ward & Emmony 1991; Philipp & Lauterborn 1998; and Kodama & Tomita 2000). The discrepancy between experiment and numerical simulations leads to the assumption that the counterjet is not a part of the bubble, but is created in the liquid by some other mechanism during bubble collapse. Its formation might be coupled to the shock wave scenario during bubble collapse. In the present study the counterjet is filmed with high spatial resolution. It is clearly visible that the counterjet consists of tiny cavitation bubbles.

Since Best (1993) has introduced a simulation method to account for the transition to toroidal bubbles, their dynamics can, in principle, be treated numerically. A simulation of the bubble collapse for some stand-off distances that are also covered by the present study was presented by Tong *et al.* (1999). For relatively low stand-offs, they find that the liquid jet, after it hits the wall, can produce a splash. The splash can have a considerable influence on the pressure that is exerted on the wall, and the first experimental evidence of such an effect was based on pressure measurements (see e.g. Shaw, Schiffers & Emmony 2001). Brujan *et al.* (2002) present high-speed photographs of toroidal bubble collapse with the splash for $\gamma = 1.1$ and 0.9, and compare them with numerical calculations. In the material presented below, the splash is investigated over a broad range of stand-off values, and resolved in some detail. Also, it is found that the bubble shapes calculated by Tong *et al.* (1999) agree with the experiment.

The bubble collapse is accompanied by a number of instabilities. The first instability is responsible for the production of the jet. It acts on a relatively large scale and does not affect the smoothness of the bubble surface. In the late phase of collapse the bubble surface becomes ruffled, and for some stand-off values a mesh-like bubble shape is observed at maximum compression. These phenomena are also thought to be due to instabilities.

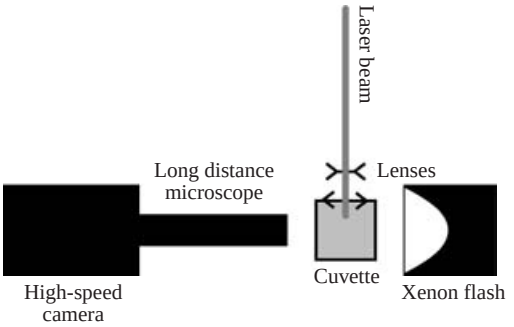

FIGURE 1. Experimental arrangement for bubble generation and observation with high-speed cinematography (top view).

2. Experiment

Figure 1 shows a sketch of the experimental arrangement used in the present study. The experiment is placed on an optic table ($4.05 \times 1.51\,\mathrm{m}^2$, TMC, MICRO-g), which is shielded by Perspex panels form contamination with dust, and constantly flooded with clean air. In the following the individual components of the experiment are described.

2.1. *Bubble generator*

For bubble production a strong laser pulse is focused by a two-lens system into a cuvette filled with water. An optical breakdown in the liquid arises, and generates a bubble that, when expanded to a large size, is mainly filled with vapour. Within limits, the bubble size can be adjusted by changing the laser energy. In the present study, however, bubbles have a maximum radius of $R_{max} = 1.5\,\mathrm{mm}$ (see § 2.1.2 for the repeatability of production of such bubbles). This size gives good results, and allows comparisons with other recent studies (e.g. Philipp & Lauterborn 1998 use a bubble size of $R_{max} = 1.45\,\mathrm{mm}$, and Shaw *et al.* 2000 use $1.2\,\mathrm{mm} \leqslant R_{max} \leqslant 1.8\,\mathrm{mm}$).

2.1.1. *Laser and focusing lenses*

Bubbles are generated with a Q-switched Nd:YAG laser beam (HY 750, Lumonics Ltd.). The laser emits pulses with a maximum energy of 740 mJ at a wavelength of 1064 nm and a pulse width of 8 ns. It is operated with a repetition rate of 1 Hz. Employing infrared filters (KG5, Schott) the laser energy is attenuated to utilize the better pulse to pulse stability at higher laser energies.

The laser pulse is focused into clean, distilled water by a two-lens system developed by Philipp (1995). The lenses are optimized to yield a short plasma length at a sufficient distance from the walls of the cuvette. The first lens is mounted outside the cuvette and can be aligned. The second lens is built into the cuvette wall. The distance of the focal spot from the second lens is 25.4 mm, the focusing angle is $2\theta = 25.1°$, and the calculated spherical aberration on the optical axis is 22 μm. Bubbles display an almost perfect spherical shape, with an initial slightly prolate deviation on the optical axis. The prolate deviation changes to a slightly oblate deviation as the bubble reaches maximum size (see Lindau 2001 for details, also see Tomita & Shima 1990). The deviations, however, are small, and bubble generation is very reproducible.

2.1.2. *Cuvette*

The internal size of the cuvette is $120 \times 95 \times 100\,\mathrm{mm}^3$ (length × width × hight). The bottom wall of the cuvette and the wall facing the laser are made of aluminium.

γ	t_{12} (μs)	γ	t_{12} (μs)	γ	t_{12} (μs)	γ	t_{12} (μs)	γ	t_{12} (μs)
∞	273	1.8	298	1.1	325	0.7	346	0.3	363
3.0	288	1.6	302	1.0	330	0.6	350	0.2	366
2.6	290	1.4	310	0.9	336	0.5	355	0.1	368
2.0	295	1.2	320	0.8	341	0.4	359		

TABLE 1. Values of $t_{12} = 2t_c k_1$ for a bubble with $R_{max} = 1.5$ mm. The k_1 values are taken from Vogel & Lauterborn (1988) and are extrapolated for $\gamma < 0.5$.

Sidewalls and the wall opposite the laser are made out of glass and allow the observation of the bubble. A plane, solid wall is inserted into the cuvette from the top, and is placed below the bubble. This wall is made out of PVC (polyvinylchloride), plain glass, or ground glass. The PVC wall is used for bubbles in side view, the plain glass for the bottom view, and the ground glass for the view at an angle. The distance from the bubble can be adjusted, and the dimensionless stand-off parameter

$$\gamma = \frac{d}{R_{max}}, \tag{2.1}$$

is defined by the maximum bubble radius R_{max} and the distance of the bubble centre from the wall at the moment of formation d. For a bubble with $R_{max} = 1.5$ mm, γ can be determined with an accuracy of about 0.1.

A PVDF (polyvinylidene fluoride) hydrophone (CERAM, sensitivity 0.4 μVPa^{-1}, band width 10 MHz, active area ca. 0.8 mm^2) is placed in the cuvette a sufficient distance from the bubble to not disturb its dynamics. The hydrophone is used to obtain the period of time t_{12} between the shock waves that are emitted at formation and at the first collapse of the bubble. In the absence of the wall, the bubble size can then be calculated using Rayleigh's formula

$$R_{max} = 1.09 \sqrt{\frac{p - p_v}{\rho}}\, t_c, \tag{2.2}$$

where $p = 98.07$ kPa is the ambient pressure, $p_v = 2.98$ kPa the vapour pressure, and $\rho = 998.2$ kg m^{-3} the density of the liquid (Rayleigh 1917). Here t_c is the collapse time for an undisturbed, spherical bubble. The collapse time near a wall is multiplied by the γ-dependent parameter $k_1 \geqslant 1$ that was empirically determined by Vogel & Lauterborn (1988), and t_{12} equals twice this time. Table 1 lists the values of $t_{12} = 2t_c k_1$ used in the present study. This time, and thereby R_{max}, is controlled via the laser energy. The jitter in t_{12} is in the order of few microseconds, and is due to unstable laser energies and variations in the initial plasma. In order to obtain constant bubble sizes, in the experiment bubble photos with a deviation of less than a microsecond from the tabulated values are selected.

A delay generator (Stanford Research Systems, Model DG 535) triggers the laser and high-speed camera. A digital sampling oscilloscope (TDS 784A, Tektronix) is used to record the signal of the hydrophone, the monitor signals of the camera, and the trigger pulses.

2.2. *Cinematographic arrangement*

Bubbles and shock waves are recorded with a system consisting of a high-speed camera, lenses, and a bright illumination. In all movies the laser pulse comes from the left.

2.2.1. *High-speed camera*

The key part of the observation system is an Imacon 468 high-speed camera (DRS Hadland LTD). In the camera the light is divided into eight separate optical paths by a pyramidal beam splitter. Eight ICCDs (intensified charge coupled devices) that are individually triggered by a 100 MHz delay generator record sequences with interframe times between several 100 μs and 10 ns. Camera gain and the delay of exposure time can be set for each individual frame. To obtain movies with more than eight frames, sequences with different delays are subsequently combined. For such movies the correctness of the series is manually cross-checked with sequences taken at lower framing rates (typically 1/4 of the original rate).

2.2.2. *Observation lenses*

Two long-distance microscopes (Questar QM 100 and Infinity K2) are alternately employed as camera lenses. The distance between bubble and lens varies between 100 and 500 mm. A maximum resolution of 1.1 μm per pixel can be achieved with the Questar microscope together with a positive Barlow lens. The mean resolution used in the present study, however, is between 2 and 3 μm per pixel.

2.2.3. *Illumination*

The cuvette is illuminated with a strong xenon flash (500 Joule, 20 μs and 50 μs FWHM, alternately) from the side opposite to the camera. The sequences shown in figure 7 are illuminated with a photo flash (Metz 36 CT 2) having a pulse width above 1 ms. Shock waves are made visible by a shadowgraph technique, placing the flash at some distance from the cuvette (>1 m) to yield an almost parallel illumination. For all other recordings the flash is situated as close as possible to the cuvette, and a ground glass plate is placed between flash and cuvette. In the sequences viewed at 45°, the ground glass is immersed into the cuvette at this angle, and the plain side serves as a wall.

3. Bubble dynamics, shock waves, and counterjet

A sequence of pictures that displays typical bubble behaviour in the last stage of collapse and in the first stage of rebound is shown in figure 2. The two assembled sequences are taken at a moderately high rate of 1 million frames per second, the stand-off parameter is $\gamma = 2.6$, and the bubble is seen from an angle of 45° above the wall. The bubble was generated 278 μs before the first frame of the movie, expanded to the maximum size of $R_{max} = 1.5$ mm, and subsequently started to collapse. In the first frame the bubble has already contracted considerably to approximately 6% of its maximum volume.

After formation a laser-generated bubble has an unruffled, smooth surface and therefore is in a way transparent. During expansion and collapse the bubble surface remains smooth. In the first frame of figure 2 such a surface is visible, and the bubble shows a small inwards dent on the side opposite the wall. As the bubble shrinks, this dent grows in width and length and develops into a liquid jet that penetrates into the bubble. Beginning with frame 6, the tip of the jet becomes visible in the interior of the bubble below the dark rim of the indentation. (Due to refraction the tip appears distorted.) Shortly before the impact of the jet on the lower bubble surface, the tip of the jet becomes visible from above, and the bubble has a bowl-like shape (frame 12). Thereafter, in rapid progression the jet and the bubble surface meet, and the bubble reaches a stage of minimum volume. This scenario is very involved and is addressed

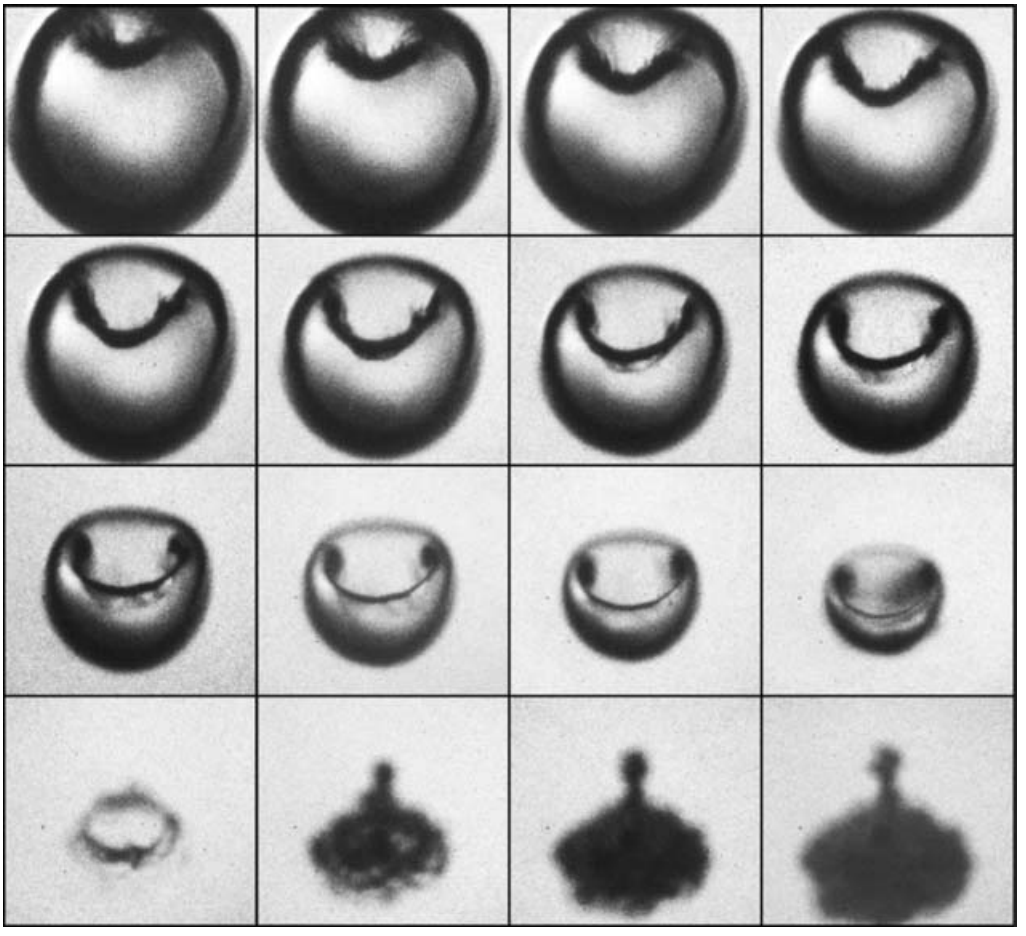

FIGURE 2. Jet and counterjet development seen at an angle of 45° from above the wall; $\gamma = 2.6$. Interframe time 1 μs, exposure time 200 ns, $R_{max} = 1.5$ mm, frame size 1.2 mm × 1.1 mm.

in more detail in § 3.1. In frame 13 the jet has completely penetrated the bubble, and made a large-area contact with the liquid below. The bubble shape is toroidal, and the bubble is in rebound; it has a rough surface and appears opaque. Then it increases in volume, and the counterjet, an upwards protrusion, becomes visible above the bubble. It is not discernible whether bubble and counterjet are connected or not. The counterjet appears rough, like the remaining bubble during rebound. As the bubble grows in volume, the counterjet gains in height, and the ruffled appearances of bubble and counterjet remain.

3.1. *Shock wave emission phase*

For $\gamma = 2.6$ the period of shock wave emission around the bubble minimum is less than 300 ns, corresponding to 0.1% of the time from bubble formation to its first minimum. The shortness of this period requires a fast means of observation. The sequence in figure 3, which is taken at the highest temporal resolution that can be obtained in the current setup, shows the bubble dynamics and the shock wave emission.

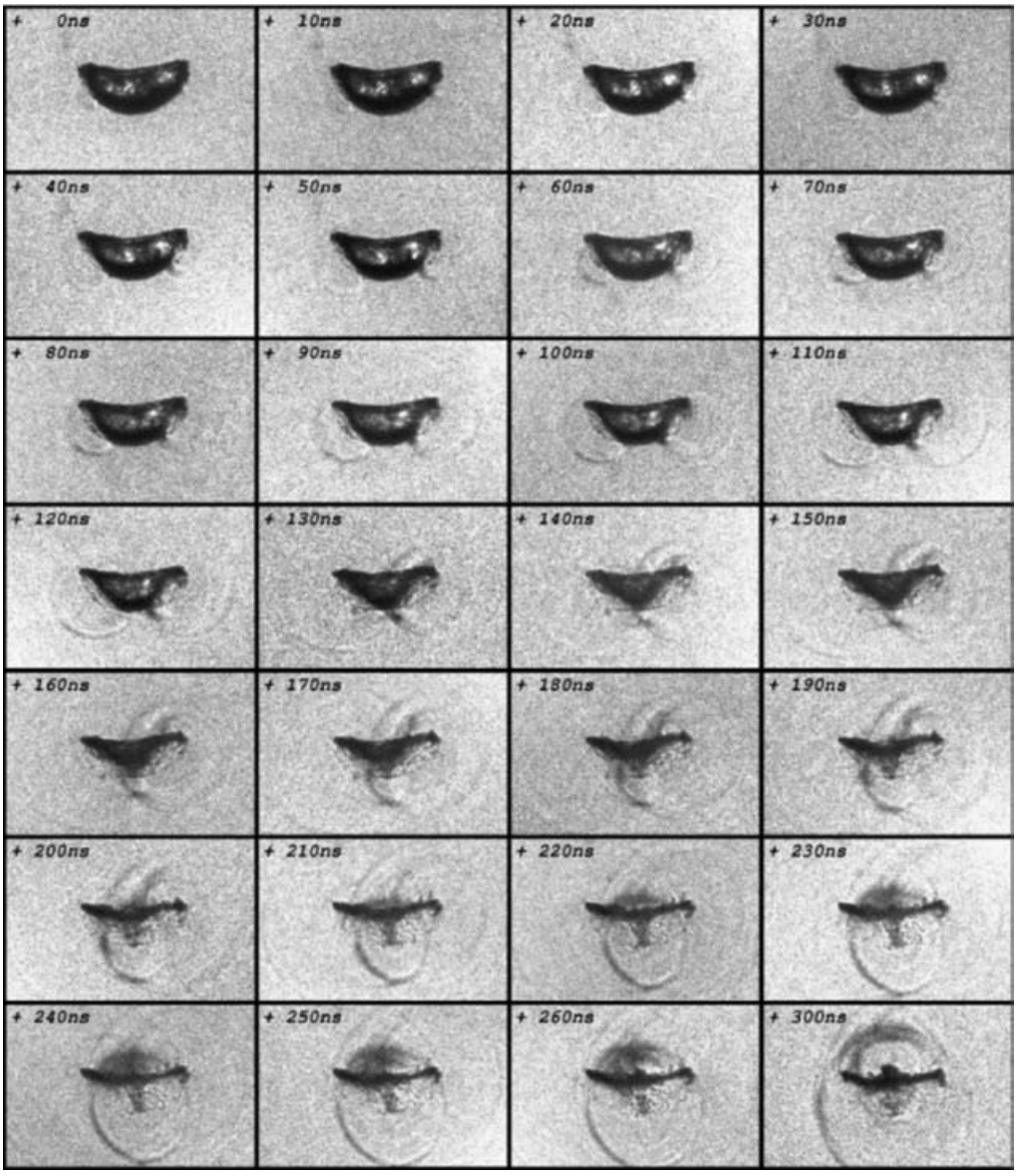

FIGURE 3. Shock wave scenario during bubble collapse filmed at 100 million frames per second; $\gamma = 2.6$. Shadowgraph, $R_{max} = 1.5\,\text{mm}$, frame size $1.3\,\text{mm} \times 0.8\,\text{mm}$. Time is displayed in the upper left corner of each frame.

3.1.1. *Shock wave scenario*

A first shock wave is released when the jet and lower bubble surface make contact, and is emitted on a ring. It expands toroidally, and is therefore called *jet torus shock wave* (names are taken from Ohl *et al.* 1999). The formation of this shock wave is easily explained by the water hammer pressure that arises during the impact. In the first row of figure 3 the development of the jet torus shock wave can be seen on the left and the right sides of the bubble, and in the following rows two 'wing'-like structures become visible on either side of the bubble as the shock wave expands.

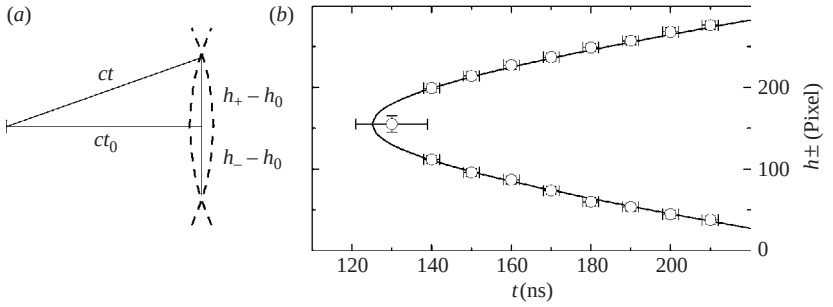

FIGURE 4. (*a*) For the heights $h_\pm$ of the upper and lower intersection points of a self-penetrating torus, $(h_\pm(t) - h_0)^2 = (ct)^2 - (ct_0)^2$ holds; c is the propagation velocity of the torus radius, t_0 the instant of time at which the self-penetration begins, and h_0 the hight of the torus centre. (*b*) $h_+(t)$, $h_-(t)$ (curve) and the measured heights (circles) are in excellent agreement. The (only) fit parameter t_0 is determined to be 124 ns (time as in figure 3). The errors are calculated from the camera resolution, and the uncertainty in t for the first height is relatively high (and possibly overestimated) since, at the beginning, the self-penetration points are masked by the bubble.

At 130 ns seemingly a second '*tip bubble shock wave*' appears at the lowest point of the bubble, and in the following frames its sideways and downwards propagation becomes visible. The downwards propagation velocity of the 'tip bubble shock wave', however, appears to be very high (at the start about 7000 m s^{-1} can be measured in the current setup, corresponding to a rather high pressure of several 10 MPa, see Cole 1965, p. 36 ff). What appeared to be a tip bubble shock wave is in fact the lower section of the inward moving part of the jet torus shock wave that has already started self-penetration. The upper section is also visible above the bubble; it is less pronounced since it first propagates in the jet funnel where it is attenuated.

The inward moving part of the toroidal shock wave converges to a point that is located in the torus centre. The instant in time at which this occurs will in the following be called t_0. After t_0, as the shock wave begins to penetrate itself, the point splits into two points moving in opposite directions. The velocities $v_+(t)$ and $v_-(t)$ of the upwards and downwards moving points, respectively, are given by

$$v_\pm(t) = \frac{\mathrm{d}}{\mathrm{d}t} h_\pm(t) = \frac{\pm ct}{\sqrt{t^2 - t_0^2}}, \tag{3.1}$$

for $t > t_0$, when we assume that after t_0 the propagation velocity c of the shock wave is constant ($c = 1490$ m s^{-1}). Figure 4(*a*) shows a sketch of the geometry, and in the figure caption a derivation of the heights $h_\pm(t)$ is given. The velocities in equation (3.1) agree with the observed velocities of the corresponding intersection points of the jet torus shock wave. Figure 4(*b*) shows a comparison of the experimental and theoretical heights of the intersection points. For $t \to t_0$ the velocities $v_\pm(t)$ diverge for geometrical reasons.

The high velocities of the intersection points do not correspond to a physical pressure. Nevertheless, the shock wave pressure at the intersection point can be very high, which is noteworthy, because the upper intersection point travels on the path on which the counterjet emerges later. As detailed in § 3.2.4, the shock wave scenario is presumably connected to the counterjet creation.

Two *compression shock waves* are emitted in rapid succession when the bubble reaches minimum size and maximum compression. The first wave becomes visible on

top of the bubble at 210 ns, and is only seen to propagate towards the top. Its origin, however, is not necessarily the high pressure inside the bubble; it might also be a part of the jet torus shock wave, which has travelled through the bubble where it was focused, delayed, and given a direction. The second wave is emitted at 240 ns and propagates in all directions.

Compression of the bubble interior can be determined from volumes V_{max} and V_{min} that are measured at maximum and minimum bubble size. For $\gamma = 2.6$ a compression of $V_{max}/V_{min}^{(2.6)} \approx 2 \times 10^4$ is observed. Note that the compression depends on the stand-off distance, and in this case is about one order of magnitude lower than it is for an undisturbed bubble (see § 4.3 for more details). It is strong enough to explain the occurrence of a high pressure at the bubble minimum, and the subsequent emission of strong compression shock waves.

The period of time between the emission of the jet torus shock wave and the compression shock waves also depends on γ, and becomes longer at lower stand-off values, which corresponds to the fact that the period of time between the meeting of the jet and the lower bubble surface and maximum compression increases in this stand-off range, as well.

3.1.2. *Bubble dynamics*

Bubble dynamics and shock waves should not be considered separately. In the same way that a high compression of the bubble interior leads to the emission of compression shock waves, the shock waves do interact with the bubble motion. The motion of a surface is affected when a shock front travels over it. In general, a high pressure exerted on the outside of a bubble should push its surface inwards. Such a motion is observed in the current scenario when the inwards moving part of the jet torus shock wave passes over the lower bubble surface, and the bubble shape changes from hemispherical towards pyramidal (see figure 3). The pyramidal shape is reached when the jet torus shock wave starts to penetrate itself (at 130 ns), followed by a change towards a ring-like structure at maximum compression (see figure 2). After this shape transformation, the bubble is in rebound and develops a counterjet.

3.2. *Counterjet*

The counterjet forms for a certain range of the stand-off parameter. Vogel *et al.* (1989) have shown that a counterjet develops only for $\gamma > 1$, which is confirmed in the present study. Also, no counterjet can be found above $\gamma \approx 3$. The counterjet emerges very rapidly and remains visible for a long period of time (compared to the collapse time). For $\gamma > 2$, however, the duration of visibility becomes shorter on increasing γ, and the counterjet is sometimes not seen when using lower framing rates.

The formation of the counterjet is coupled with an impact of the jet on the lower bubble surface. For high values of γ the impact is weak, or does not happen, and no counterjet arises; and for stand-off values below unity, no counterjet is found because the bubble touches the wall during expansion, and the jet directly impinges on the wall, or on a thin sheet of fluid.

3.2.1. *Formation velocity*

To quantify the formation velocity of the counterjet, the stand-off parameter is varied systematically, and the first 8 μs of the counterjet onset are filmed in side view. Figure 5 shows four sequences of counterjet formation for different stand-offs. In the first frame of each row the bubble is seen shortly after the shock wave emission at maximum compression. Beginning with the second frame the counterjet becomes

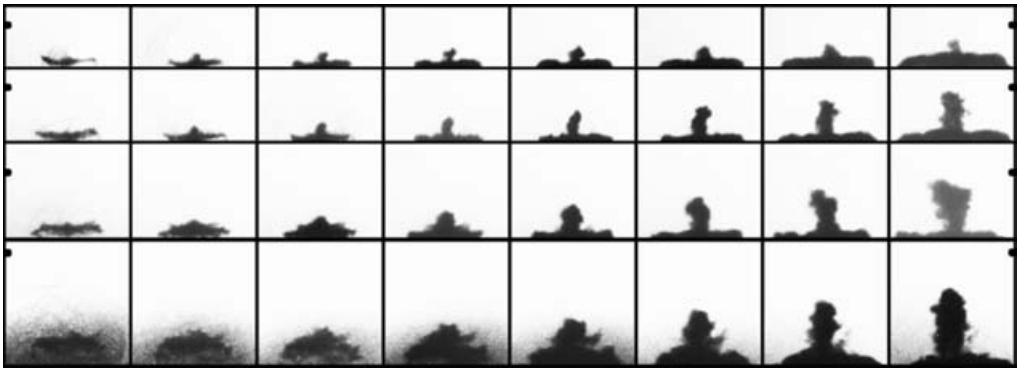

FIGURE 5. Onset of the counterjet for $\gamma = 2.6$, 2.2, 1.8 and 1.4 (top to bottom) 10, 120, 250, 500, 1000, 2000, 4000 and 8000 ns after shock wave emission. Side view, exposure time 10 ns, $R_{max} = 1.5$ mm, frame width 0.97 mm. The marks on the left of the first and the right of the last frame of each sequence indicate the horizontal position of the bubble creation location.

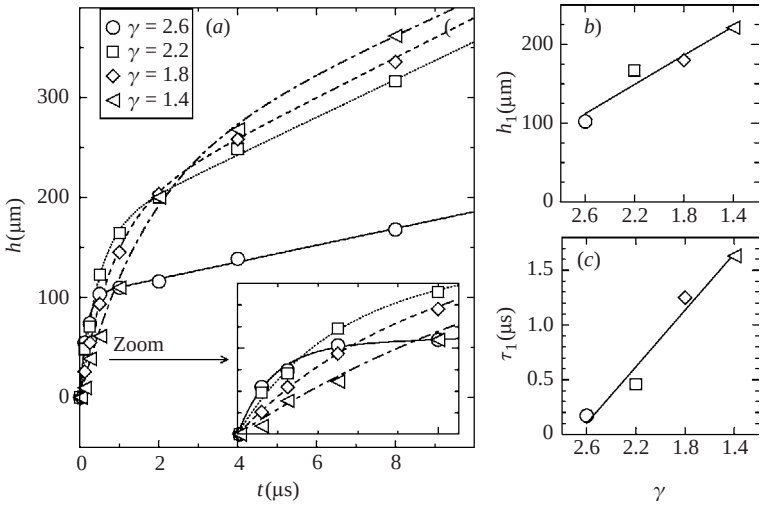

FIGURE 6. (*a*) Counterjet height for various γ. The zoomed inset displays the first 1.1 μs. Symbols show the heights measured in figure 5, the lines show fits of function (3.2) to the measured values. (*b*, *c*) Values of h_1 and τ_1 vs. γ (see text).

visible, and in the following frames it grows in width and height. Its maximum size increases as γ is decreased. The height $h(t)$ of the counterjet is measured relative to the upper bubble surface in the first frame of each row, and the values are plotted in figure 6(*a*). A function (3.2) is fitted to the measured values, and displayed as lines. A discussion of the fit parameters is given below.

The evolution of counterjet height is modelled with

$$h(t) = h_{max} - h_1 \exp(-(t - t_0)/\tau_1) - (h_{max} - h_1) \exp(-(t - t_0)/\tau_2), \quad t \geqslant t_0. \qquad (3.2)$$

This empirical function has two exponential terms, which reflect the observation that the counterjet emerges very rapidly, while it can be seen over a long period of time. The first exponential term describes the fast growth during the initial counterjet formation period. The growth velocity at formation is represented by a time constant

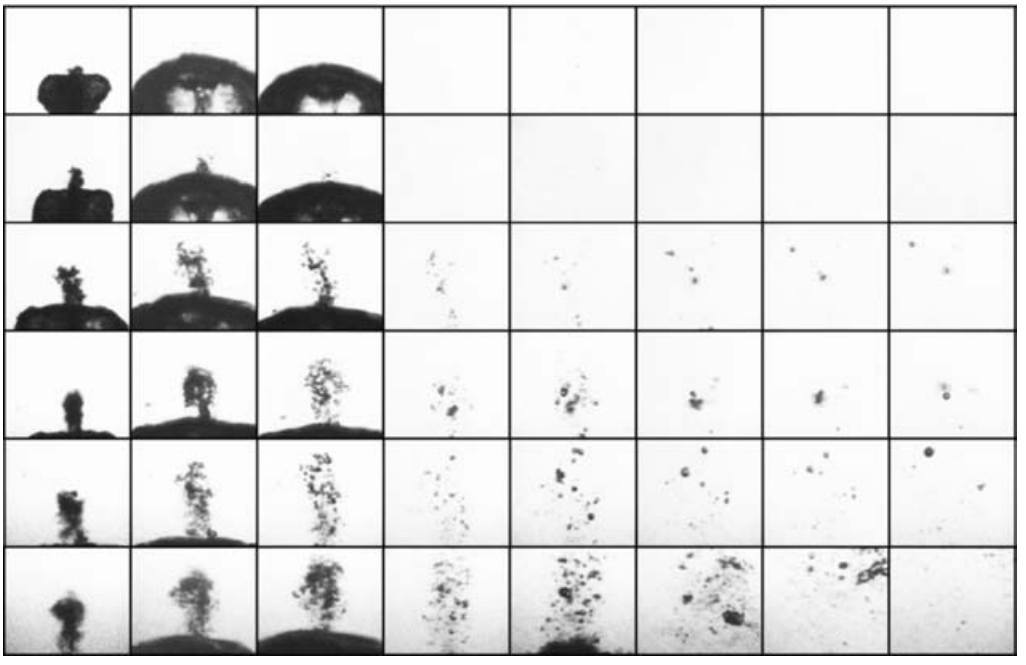

FIGURE 7. Evolution of the counterjet for $\gamma = 2.6, 2.2, 1.8, 1.6, 1.4$ and 1.2 (top to bottom) 5, 50, 100, 200, 300, 500, 700 and 1100 µs after its onset. Side view, exposure time 30 ns, $R_{max} = 1.5$ mm, frame size 1.42 mm × 1.21 mm.

τ_1 in the order of 1 µs. The counterjet emerges at $t = t_0$, and at $t - t_0 = 2.3\tau_1$ its height is $h = 0.9h_1$. The second term adds a slow growth with a time constant τ_2 of approximately 40 µs; the maximum counterjet height h_{max} is in the order of 1 mm (see figure 7).

The graphs of function (3.2) are in perfect agreement with the measured values in figure 6(*a*). The parameter t_0 is in the order of nanoseconds, which is expected since the first frames of figure 5 approximately show the beginning of the counterjet onset. The γ-dependences of h_1 and τ_1 are shown in figure 6(*b*, *c*). At $\gamma = 2.6$, $h_1 = 100$ µm but doubles for $\gamma = 1.4$, and the time parameter $\tau_1 = 170$ ns but increases about ten times as γ is reduced to 1.4, which means that on reducing the stand-off the formation velocity decreases while the counterjet height becomes larger.

3.2.2. *Duration of appearance*

In the following the counterjet evolution is investigated over a period of 1.1 ms, which is two orders of magnitude longer than in § 3.2.1. In figure 7 six sequences of the counterjet evolution are shown for different stand-offs. For $\gamma = 2.6$ the counterjet vanishes 50 µs after its onset, because at rebound the bubble grows over the counterjet (second frame, first row), but for $\gamma = 2.2$ it is large enough that it survives the rebound of the bubble. Nevertheless, the conterjet intensity decreases in time, and 100 µs after the onset it is barely visibility (third frame, second row). For lower stand-off values the counterjet remains visible over the whole period. The maximum height for $\gamma = 1.8$ is 1 mm, and as γ is decreased the final height increases slightly. Also, for a given stand-off value, the growth velocity eventually becomes slower; for $\gamma = 1.4$ this velocity is 6.7 m s^{-1} between the first two frames and 1.7 m s^{-1} between the second and third frame.

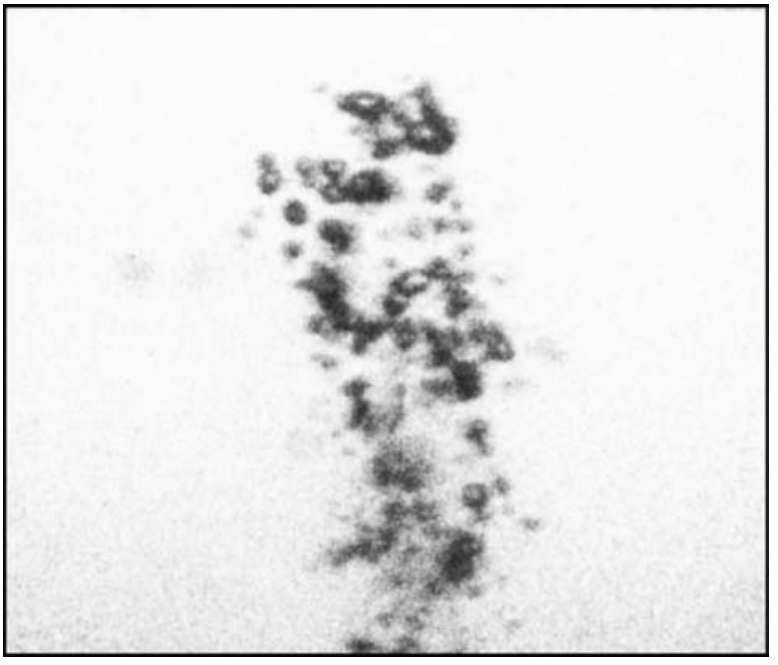

FIGURE 8. Counterjet 100 μs after its onset. Blow-up of the third frame, fifth row of figure 7; $\gamma = 1.4$, frame size 1.42 mm × 1.21 mm.

3.2.3. *Consistence*

Shortly after its onset the counterjet appears ruffled and opaque with a consistency similar to that of a bubble during rebound. In contrast to the bubble, however, its appearance modifies as the counterjet grows: its volume increases while the amount of material appears to stay approximately the same. The counterjet decays into its constituents and micro-bubbles are formed, which can be seen in the blow-up in figure 8. In this image several hundred bubbles with radii up to 50 μm are visible.

3.2.4. *Creation mechanism*

A characteristic time for the bubble dynamics is the collapse time t_c, which is in the order of 150 μs. The time τ_1, which is characteristic for the onset of the counterjet, is two to three orders of magnitude shorter. This means that the counterjet is created by a comparatively fast mechanism. Such a mechanism might be cavitation inception that follows the self-penetration of the jet torus shock wave. It is observed experimentally that the counterjet forms exactly on the path along which the intersection points of that shock wave move. The high pressure at the intersection points is presumably followed by a tension wave which gives rise to cavitation inception and so forms the counterjet. The counterjet, however, is only seen above the bubble. A hypothetical counterjet formation below the bubble, induced by the lower intersection, is impossible since during rebound the bubble grows with a high velocity towards the wall. The bubble expands over the hypothetical location and thus prohibits cavitation inception, similar to the extinction of the counterjet above the bubble for $\gamma > 2$.

A comparable shock wave scenario with subsequent cavitation inception at the tip of a glass fibre has been recently reported by Frenz, Paltauf & Schmidt-Kloiber (1996), and was repeated in our laboratory by Brendel (1998). In such experiments

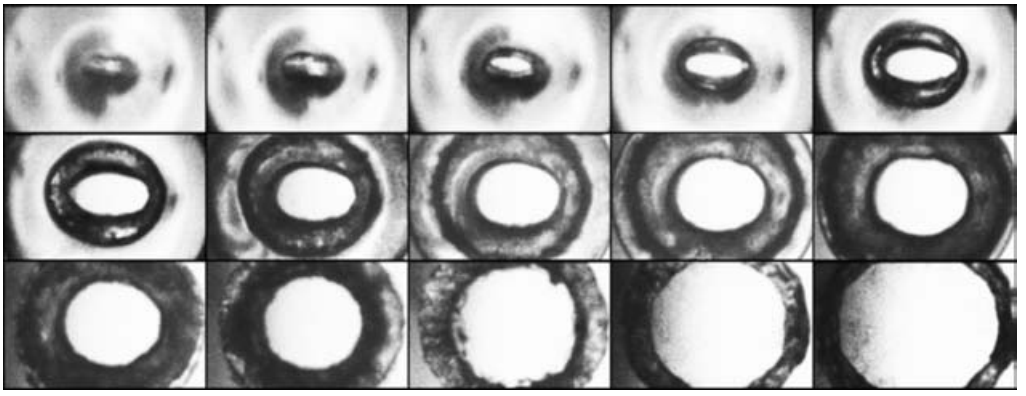

FIGURE 9. Transition to the toroidal bubble shape. Bottom view (through the wall); $\gamma = 0.9$, interframe time 2 µs, exposure time 10 ns, R_{max}=1.5 mm, frame size 1.64 mm × 1.03 mm.

the fibre is used to deliver a short laser pulse into an absorbing liquid, where a strong pressure pulse is emitted and a toroidally expanding stress wave forms by acoustic diffraction. On the intersection line of the toroidal wave, cavitation inception similar to the counterjet formation is found. Since the length and time dimensions involved are similar, this proves that counterjet formation by the above-mentioned mechanism is possible.

4. Toroidal bubble dynamics and compression

When a bubble is created close to the wall (for γ below unity) no counterjet emerges, and we are left only with a toroidal bubble after the jet impacts on the wall or a thin separating sheet of fluid. For stand-offs above 0.6 such bubbles produce a splash. Also, they have a relatively low compression, and an increasing major torus radius at the minimum when γ is decreased. Below 0.6 the compression is higher, the major torus radius decreases, no visible splash occurs, and the bubble shape becomes mesh-like at the minimum.

4.1. *Toroidal bubble dynamics in the splash regime* ($\gamma > 0.6$)

The sequence of pictures in figure 9 shows the last stage of collapse for a bubble with $\gamma = 0.9$ in bottom view, through the wall. The bubble was generated 349 µs before the first frame, expanded to the maximum size of $R_{max} = 1.5$ mm and subsequently started to collapse, developing a liquid jet, which is directed towards the wall. In the first frame the bubble is separated from the wall only by a thin sheet of fluid. The liquid jet has penetrated considerably into the bubble and between the first and second frames impacts on the wall, producing a more or less toroidal bubble shape. The boundary of the impact region of the jet on the wall appears darker than the surroundings. It is first oval and then becomes circular. The fluid of the tip of the jet flows radially outwards into the space between the bubble and wall, producing a splash that can be seen beginning in frame 3 as a dark ring at the front of the outwards flow. In the following frame the splash becomes more pronounced. It emerges because the radial outwards flow meets the inwards motion of liquid induced by the collapsing bubble. The splash is projected from the thin liquid layer on the wall surrounding the jet, moving in a direction opposite to that of the jet (Tong *et al.* 1999). After its production the splash widens and moves radially outwards (between frame 4 and

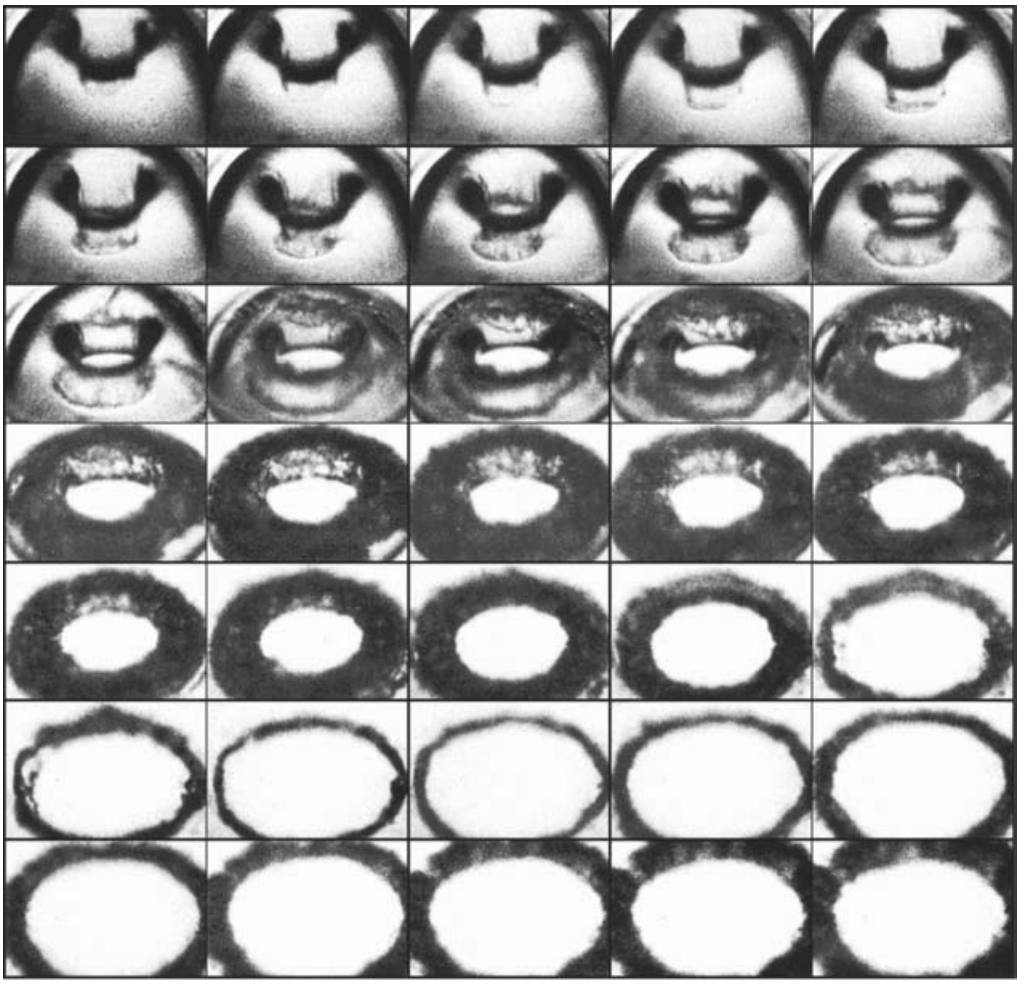

FIGURE 10. Transition to the toroidal bubble shape, seen at 45° from the wall. $\gamma = 0.8$; interframe time 1 μs, exposure time 200 ns, R_{max}=1.5 mm, frame size 1.68 mm × 1.15 mm.

frame 10). In frame 9 the width of the splash is 120 μm and its outwards velocity is 46 m s^{-1}. In their numerical simulation, Tong *et al.* (1999) find a similar velocity of 45 m s^{-1}, and a splash width of about 160 μm for $\gamma = 0.92$. (The higher splash width in the simulation might be due to the slightly higher stand-off value.) Considering the assumptions made in the numerical simulations, those results are in good agreement with the bubble shapes we find in the experiment.

The bubble in figure 10 is shown at an elevated angle of 45° from above the wall. The framing rate is higher, and the stand-off lower than in the previous figure. In the first frame the bubble has a smooth surface, and the liquid jet has again advanced considerably into the bubble. Then the jet continues its motion and in the fourth frame impacts on the wall, which can be seen from the flattening of the tip of the jet and the subsequent radial spreading of the liquid along the surface. From now on the bubble is toroidal, and the fluid of the jet flows radially outwards and forms a splash, which is clearly visible in the second row. The splash width is approximately 90 μm, and thinner than for $\gamma = 0.9$, while its velocity (48 m s^{-1}) is nearly the same,

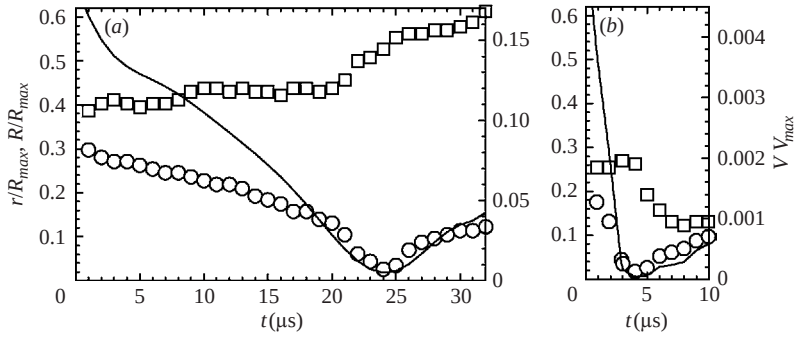

FIGURE 11. Development of major (squares) and minor (circles) torus radii, and bubble volume (solid line) after jet impact on the wall for (*a*) $\gamma = 0.8$, and (*b*) $\gamma = 0.3$.

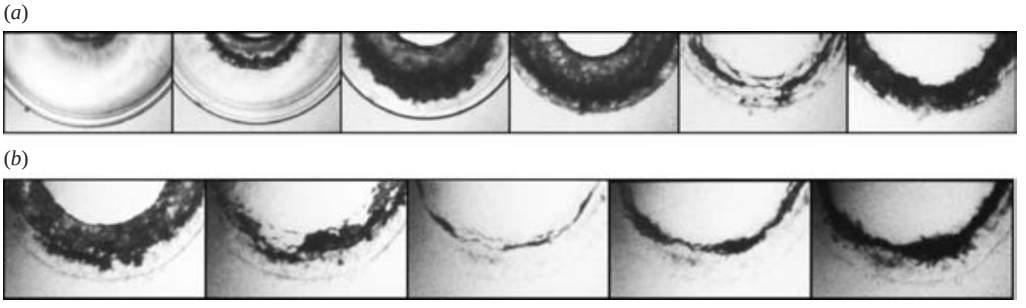

FIGURE 12. Toroidal bubble collapse, half of the bubble in bottom view; $\gamma = 0.7$, R_{max}=1.5 mm. (*a*) Interframe time 5 μs, frame size 1.67 mm × 0.99 mm. (*b*) Interframe time 1 μs, frame size 1.68 mm × 0.99 mm.

in agreement with the simulations of Tong *et al.* (1999) that yield a splash width of 97 μm, and a similar velocity (46 m s^{-1}) for $\gamma = 0.81$ (see also Pearson, Blake & Otto 2001). The splash moves outwards until it meets the outer rim of the bubble, and at the same time the torus bubble continues contracting. During contraction the minor torus radius r with its centre inside the bubble shrinks, while the major torus radius R with its centre in the liquid grows slightly. (In figure 11(*a*) both torus radii are plotted together with the bubble volume $V = 2\pi Rr^2$.) The minimal bubble volume is reached in the second frame of the sixth row in figure 10, where the torus radii of the bubble are 0.73 mm and 0.04 mm, respectively, resulting in a maximum volume compression of only 600. Beginning with the third frame, sixth row, the bubble is rebounding, and both torus radii grow. The bubble subsequently displays a rough surface and appears opaque. The transition from a smooth to a rough bubble surface starts in the part of the bubble near the wall and moves with the splash. From frame 3, row 4, onwards the bubble surface is rough, and starts becoming distorted; also it becomes unstable and tends to split. In the first frame, seventh row, some fragmentation of the bubble is visible.

Two distinct differences with the dynamics for higher stand-offs are visible for $\gamma = 0.7$ (figure 12). First, at the outer rim of the toroidal bubble a number of concentric rings emerge, which can bee seen from the first frame of figure 12(*a*) onwards. The rings might be due to the closer proximity of the bubble to the wall. When the bubble contracts, a portion near to the wall is hindered in its motion

and produces a flat ring at the outer rim. Some rings, however, may also be due to reflection and diffraction of the light by the bubble. The second difference becomes visible shortly before the bubble reaches maximum compression. The stability of the bubble surface is weaker than for higher higher stand-offs, and the bubble starts to disintegrate into a structure of thin filaments that can be seen in the fifth frame. Before the disintegration begins a splash is visible (frames 1 to 4). It is less pronounced than for higher γ-values, has an approximate width of 45 μm in frame 2, and widens considerably in the following frames. Its velocity (about $30\,\mathrm{m\,s^{-1}}$) is lower than for higher stand-off values. (A direct comparison to the study of Tong *et al.* 1999 is not possible, because they do not cover stand-offs below 0.8.) As before, the bubble surface becomes ruffled when the splash moves over it. In figure 12(*b*) the disintegration process is shown with a higher framing rate. In the first frame the bubble has a toroidal shape and a rough surface, its outer rim is ruffled, and it is surrounded by a very thin ring. The second frame corresponds to about the fifth frame of figure 12(*a*). As the torus contracts it produces an irregular structure, located between two concentric circles. The minimum volume is reached in frame 3, where the bubble is highly compressed and has the shape of a thin ring of uneven thickness. This ring is much thinner than for higher stand-offs (compare figure 10). In frames 4 and 5 the bubble is rebounding.

4.2. *Toroidal bubble dynamics in the high compression regime* ($\gamma < 0.6$)

For stand-off values below 0.6 the bubble shape at maximum compression differs considerably from the shape at higher γ-values, shown in figure 13 for $\gamma = 0.5$. In the first frame of figure 13(*a*) the bubble has a ring at its outer rim, similar to that for $\gamma = 0.7$. The ring is visible throughout the first four frames of the sequence. In frame 3 the liquid jet has begun to spread between the bubble and the wall, but no splash is visible, which is plausible because the bubble has possibly already made a larger contact with the wall. The liquid that comprised to the jet, moves outwards inside the bubble along the surface, and separates the bubble from the wall. It meets the inwards moving liquid of the contracting bubble only when it has reached the outer rim in contact with the surface. In the fourth frame the outward motion has continued, and the bubble surface has become rough where the fluid has passed over it. The roughness is less pronounced than for higher stand-offs. In frame 5 the outwards moving fluid has disconnected the bubble and wall, and maximum compression is reached between the fifth and sixth frames. (Thereafter the bubble is rebounding, during which it has a cloud-like appearance.) Figure 13(*b*) displays these dynamics in some detail at a higher framing rate. The third frame corresponds to the fifth frame, and the last frame to the sixth frame of figure 13(*a*). In the first frame the bubble, which is still contracting, has just become disconnected from the wall. During the contraction period in frames 1 to 3, the inwards movement of the outer part of the bubble is slightly higher than the outwards movement of the inner part, and beginning in frame 2, the outer surface of the bubble becomes unstable and develops a rough shape. The structure is emphasized in frame 3, and might be due to a kind of Rayleigh–Taylor mixing (see e.g. Dimonte & Schneider 2000). In frame 4, a shape appears that is not observed for higher stand-off values. Here, the torus bubble has dissolved into a very thin, mesh-like shape that covers the space where the bubble had been. The volume has decreased considerably, and the bubble remains barely visible. At the start of rebound its shape changes only slightly (frame 5), and as the bubble volume increases the bubble shape remains mesh-like, until a typical cloud-like appearance is obtained in frame 8.

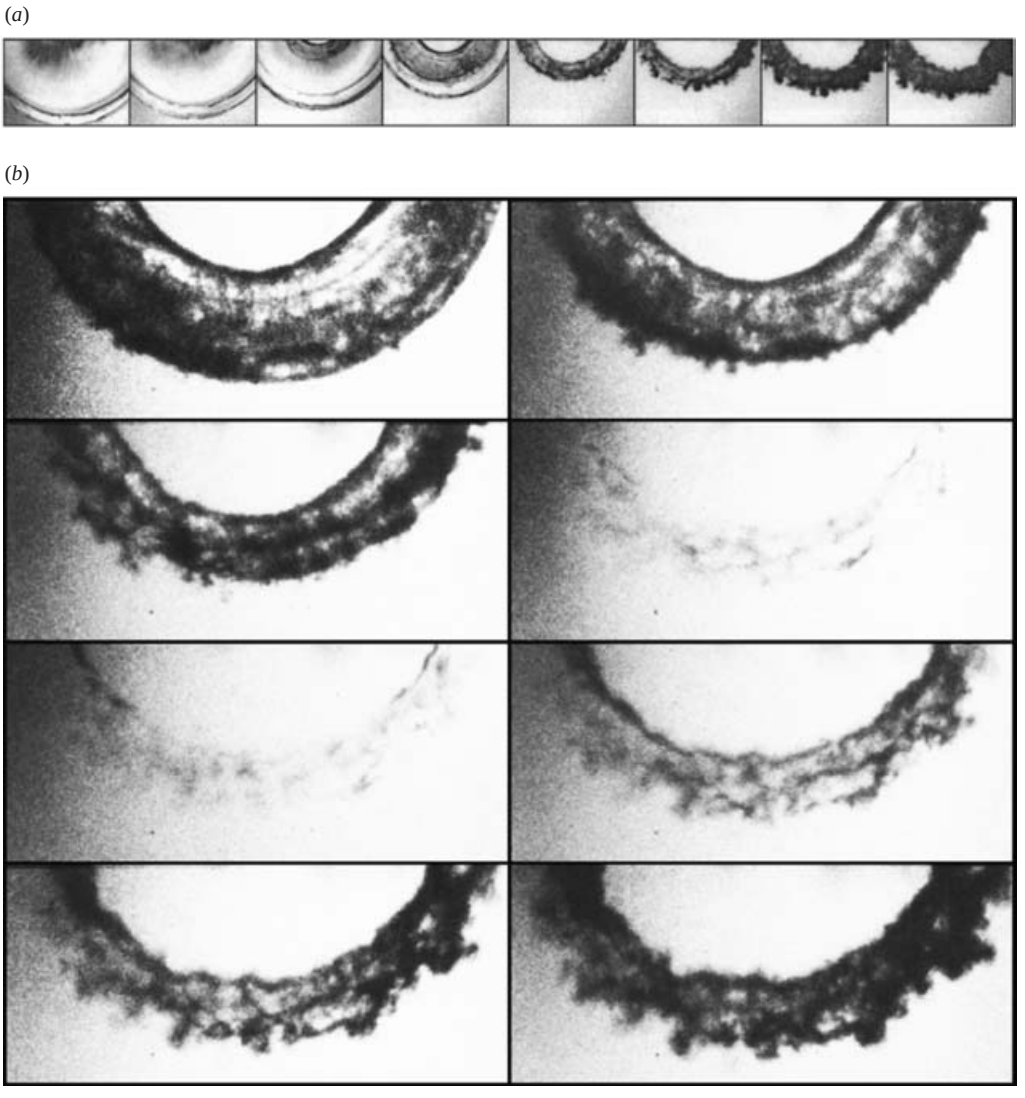

FIGURE 13. Toroidal bubble collapse, half of the bubble is seen in bottom view; $\gamma = 0.5$. (*a*) Interframe time 5 μs, exposure time 10 ns, frame size 1.70 mm × 1.15 mm. (*b*) Interframe time 1 μs, exposure time 10 ns, frame size 1.73 mm × 0.76 mm.

For $\gamma = 0.4$ the bubble motion before maximum compression is faster than for higher stand-off values. The jet impact on the wall can be seen in the first frame, second and third rows, of figure 14. During contraction both torus radii shrink considerably, and maximum compression is reached in frame 4 of the second and third rows. As for $\gamma = 0.5$, the bubble shape during this stage is mesh-like. On rebound the bubble is opaque and has a typical cloud-like appearance (fifth frame, second and third rows). For lower stand-off values the period of time between jet impact on the wall and maximum compression becomes even shorter, and the bubble motion during this time becomes faster, which can be seen, e.g., when comparing the major and minor torus radii for $\gamma = 0.8$ to the values for $\gamma = 0.3$ in figure 11(*a*) and 11(*b*), respectively.

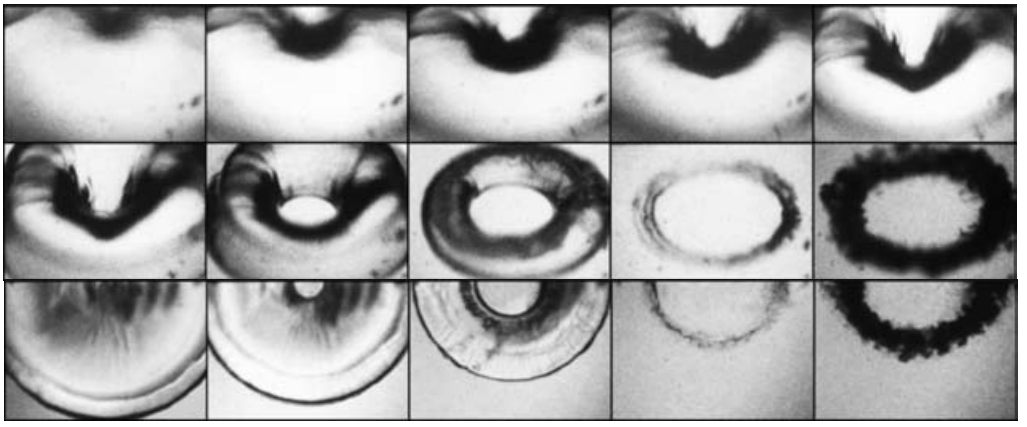

FIGURE 14. Toroidal bubble collapse, seen at an angle of 45° from the wall (1st and 2nd rows) and half of the bubble in bottom view (3rd row); $\gamma = 0.4$. Interframe time 5 μs, $R_{max} = 1.5$ mm, frame width 1.69 mm.

4.3. *Compression*

Compression is believed to play an important role in the understanding of the overall bubble dynamics. As a result of the relatively poor resolution in space and time that had been achieved in earlier experiments, however, some compression values that have been presented in the literature are not very accurate. To obtain reliable compression values, we measure the torus radii from high-speed sequences with an interframe time of 1 μs and a spatial resolution of few micrometres. The radii are normalized with respect to the maximum radius R_{max}, and presented in figure 15(*a*). In the range of $0.1 < \gamma < 1.2$, the major torus radius R has a maximum at $\gamma = 0.7$, and thereafter monotonicaly decreases for $\gamma \to 0$ and $\gamma \to \infty$. The major torus radii that are presented here are in excellent agreement with the values given by Tomita & Shima (1986). The minor torus radius r also depends on γ, and has a maximum at $\gamma = 1.0$. For stand-off values below 0.6 the bubble shape at maximum compression is not truly torus-like, because the bubble has a mesh-like appearance. Therefore, no minor torus radius is plotted in this γ-range.

In figure 15(*b*) the maximum volume compression $V_{max}/V_{min}^{(\gamma)}$ is plotted. $V_{max} = \frac{4}{3}\pi R_{max}^3 = 14.1\,\mathrm{mm}^3$ is the volume at maximum, and $V_{min}^{(\gamma)} = 2\pi^2 R r^2$ is the torus volume at minimum bubble size. The compression values are presented together with error bars, which are calculated using standard error propagation. The standard deviations in R and r are obtained from the photographs by repeated measurements. The errors in the compression values mainly depend on the accuracy with which the minor torus radius can be determined. For $\gamma \leqslant 0.5$ no minor torus radius is available, and compression values in this stand-off range are estimated by use of the minor torus radius for $\gamma = 0.6$ (i.e. $r \approx 7\,\mu\mathrm{m}$). This approximation might be justified by the observation that for $\gamma = 0.7$ the minor torus radius is similar to that for $\gamma = 0.6$, and is also supported by the observed bubble shapes. The values calculated this way (open circles in figure 15*b*), however, are high and might be overestimated for $\gamma \leqslant 0.3$. The errors in this stand-off range cannot be determined, and are believed to be higher than for the other compression values, so the values (open circles) are presented without error bars.

At $\gamma = 1.0$ the volume compression has an absolute minimum slightly above 100. For $\gamma \to 0$ compression increases by two to three orders of magnitude. Also for

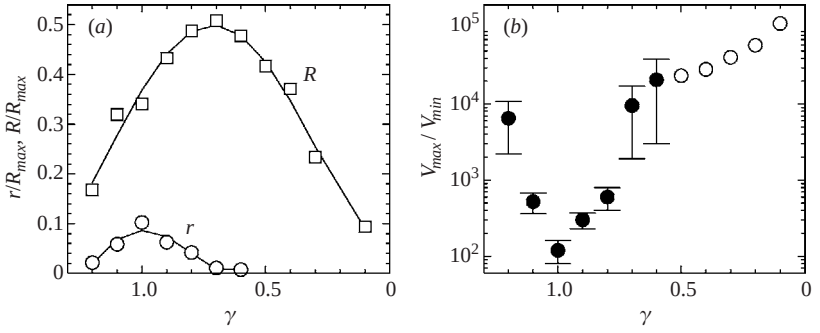

FIGURE 15. (*a*) Major and minor torus radii at minimum bubble size, relative to R_{max}. (*b*) Volume compression at minimum bubble size (see text).

$\gamma \to \infty$ a high increase in the compression is observed, which continues beyond $\gamma = 1.2$ (not plotted). For $\gamma = 2.6$ compression is 2×10^4, and for an undisturbed, spherical bubble a compression of 2×10^5 is measured (see Lindau 2001 for more details).

The dependence of the volume compression on the stand-off can be understood in a heuristic manner. A bubble that has been produced at a large distance from the wall has a very high compression, because during collapse the flow of the surrounding liquid is directed into a small region, giving rise to a strong energy focusing and high volume compression. For lower stand-off values the bubble motion is less spherical, and more energy is used up in the jet flow and associated phenomena. Therefore, compression becomes lower until at $\gamma = 1$ the bubble makes contact with the wall. When the stand-off distance is further decreased, the bubble approaches an almost hemispherical shape, leading to a later development of the jet, and a greater energy focusing during collapse, which explains the increase of the volume compression for $\gamma \to 0$.

5. Conclusions

The dynamics of a laser-generated cavitation bubble near a flat wall has been studied experimentally. Such bubbles have a maximum size in the order of millimetres and display very fast dynamics during the intense collapse. Because of the anisotropic boundary condition that is induced by the wall, bubble dynamics is essentially aspherical. The collapse of these bubbles has been the subject of many previous investigations, and some references to preceding studies have been cited in the introduction. In the present study, investigations have been carried out with unprecedented temporal and spatial resolution. This has become possible by employing the most modern experimental means, namely high-speed cinematography with an interframe time of 10 ns and long-distance microscopy.

The first part of the study is concerned with the shock waves that are emitted at the first bubble collapse, and the subsequent appearance of the counterjet. A counterjet only occurs when the stand-off distance of the bubble centre from the wall at formation is higher than the maximum radius of the bubble. The second part of the study is concerned with the mainly toroidal bubble collapse at lower stand-off distances.

An understanding of the shock waves is important since this knowledge might enhance our understanding of the erosion process. Also, shock waves might be responsible for the formation of the counterjet. A counterjet is found in many situations

where aspherical bubble collapse occurs. It is easily reproducible in bubble collapse near a solid wall, but is also observed in other conditions (e.g. near a gelatin surface, Kodama & Tomita 2000). Counterjet formation may be considered as a bubble nuclei generation mechanism. It leads to a proliferation of tiny bubbles that are not split off from the main bubble. In that sense, the counterjet is not part of the bubble.

The toroidal bubble dynamics has been studied in detail for stand-off values between 1.2 and 0.1. When the liquid jet meets the sheet of fluid that separates bubble and wall a splash emerges that moves radially outwards below the bubble. The splash diameters are similar to, and its velocities are in good agreement with, the numerical simulations of Tong *et al.* (1999). For stand-off values below 0.6 the sheet of fluid between the bubble and wall is thin, and no splashing occurs. The maximum volume compression of the bubble has a minimum for $\gamma = 1.0$ and increases dramatically for $\gamma \to 0$, which is most likely due to a more hemispherical collapse during which the liquid flow is directed into a small region on the wall.

The study raises a number of questions on the behaviour of the counterjet that might be of interest for future experiments. They include the dependence of the counterjet height, and the number, size, and lifetime of the generated bubbles on, for example, the ambient pressure, and the gas content of the liquid.

We are grateful to the members of the Cavitation Group at the Drittes Physikalisches Institut, Göttingen, for a number of inspiring discussions and to Reinhard Geisler for help with the image processing software. O.L. also thanks Antony Pearson for some helpful conversations. Financial support by the Deutsche Forschungsgemeinschaft (contract LA-268/22-1) and the Bundesministerium für Bildung und Forschung (contract 13 N7908) is acknowledged.

REFERENCES

Akhatov, I., Lindau, O., Topolnikov, A., Mettin, R., Vakhitova, N. & Lauterborn, W. 2001 Collapse and rebound of a laser-induced cavitation bubble. *Phys. Fluids* **13**, 2805–2819.

Akmanov, A. G., Ben'kovskii, V. G., Golubnichii, P. I., Maslennikov, S. I. & Shemanin, V. G. 1974 Laser sonoluminescence in a liquid. *Sov. Phys. Acoust.* **19**, 417–418.

Baghdassarian, O., Chu, H.-C., Tabbert, B. & Williams, G. A. 2001 Spectrum of luminescence from laser-created bubbles in water. *Phys. Rev. Lett.* **86**, 4934–4937.

Benjamin, T. B. & Ellis, A. T. 1966 The collapse of cavitation bubbles and the pressure thereby produced against solid boundaries. *Phil. Trans. R. Soc. Lond.* A **260**, 221–240.

Best, J. P. 1993 The formation of toroidal bubbles upon the collapse of transient cavities. *J. Fluid Mech.* **251**, 79–107.

Blake, J. R., Hooton, M. C., Robinson, P. B. & Tong, R. P. 1997 Collapsing cavities, toroidal bubbles and jet impact. *Phil. Trans. R. Soc. Lond.* A **355**, 537–550.

Brendel, T. 1998 Experimentelle Untersuchungen zur thermoelastischen Absorption bei 531 nm. Master thesis, Georg-August-Universität, Göttingen.

Brujan, E. A., Keen, G. S., Vogel, A. & Blake, J. R. 2002 The final stage of the collapse of a cavitation bubble close to a rigid boundary. *Phys. Fluids* **14**, 85–92.

Buzukov, A. A. & Teslenko, V. S. 1971 Sonoluminescence following focusing of laser radiation into liquid. *JETP Lett.* **14**, 189–191.

Cole, R. H. 1948 *Underwater explosions.* Princeton University Press, p. 36 ff.

Dimonte, G. & Schneider, M. 2000 Density ratio dependence of Rayleigh–Taylor mixing for sustained and impulsive acceleration histories. *Phys. Fluids* **12**, 304–321.

Frenz, M., Paltauf, G. & Schmidt-Kloiber, H. 1996 Laser-generated cavitation in absorbing liquid induced by acoustic diffraction. *Phys. Rev. Lett.* **76**, 3546–3549.

Harrison, M. 1952 An experimental study of single bubble cavitation noise. *J. Acoust. Soc. Am.* **24**, 776–782.

Kling, C. L. & Hammitt, F. G. 1972 A photographic study of spark-induced cavitation bubble collapse. *Trans. ASME* D: *J. Basic Engng* **94**, 825–833.

Kodama, T. & Tomita, Y. 2000 Cavitation bubble behavior and bubble-shock wave interaction near a gelatin surface as a study of *in vivo* bubble dynamics. *Appl. Phys.* B **70**, 139–149.

Kornfeld, M. & Suvorov, L. 1944 On the destructive action of cavitation. *J. Appl. Phys.* **15**, 495–506.

Lauterborn, W. 1972 High-speed photography of laser-induced breakdown in liquids. *Appl. Phys. Lett.* **21**, 27–29.

Lauterborn, W. 1974 Kavitation durch Laserlicht. *Acustica* **31**, 52–78.

Lauterborn, W. & Bolle, H. 1975 Experimental investigations of cavitation-bubble collapse in the neighbourhood of a solid boundary. *J. Fluid Mech.* **72**, 391–399.

Lindau, O. 2001 Untersuchungen zur lasererzeugten Kavitation. PhD thesis, Georg-August-Universität, Göttingen.

Naudé, C. F. & Ellis, A. T. 1961 On the mechanism of cavitation damage by nonhemispherical cavities in contact with a solid boundary. *Trans. ASME* D: *J. Basic Engng* **83**, 648–656.

Ohl, C. D., Kurz, T., Geisler, R., Lindau, O. & Lauterborn, W. 1999 Bubble dynamics, shock waves and sonoluminescence. *Phil. Trans. R. Soc. Lond.* A **357**, 269–294.

Ohl, C. D., Lindau, O. & Lauterborn, W. 1998 Luminescence from spherically and aspherically collapsing laser induced bubbles. *Phys. Rev. Lett.* **80**, 393–396.

Ohl, C. D., Philipp, A. & Lauterborn, W. 1995 Cavitation bubble collapse studied at 20 million frames per second. *Ann. Physik* **4**, 26–34.

Pearson, A., Blake, J. R. & Otto, S. R. 2001 Computational modelling of bubbles near boundaries. In *Computational Modelling of Bubbles near Boundaries* (ed. P. J. Harris), pp. 37–46. University of Brighton Press.

Philipp, A. 1995 Kavitationserosion durch lasererzeugte Einzelblasen. PhD thesis, Technische Hochschule Darmstadt.

Philipp, A. & Lauterborn, W. 1998 Cavitation erosion by single laser-produced bubbles. *J. Fluid Mech.* **361**, 75–116.

Plesset, M. S. & Chapman, R. B. 1971 Collapse of an initially spherical vapour cavity in the neighbourhood of a solid boundary. *J. Fluid Mech.* **47**, 283–290.

Rayleigh, Lord 1917 On the pressure developed in a liquid during the collapse of a spherical cavity. *Phil. Mag.* **34**, 94–98.

Shaw, S. J., Jin, Y. H., Schiffers, W. P. & Emmony, D. C. 1996 The interaction of a laser-generated cavity in water with a solid surface. *J. Acoust. Soc. Am.* **99**, 2811–2824.

Shaw, S. J., Schiffers, W. P. & Emmony, D. C. 2001 Experimental observations of the stress experienced by a solid surface when a laser-created bubble oscillates in its vicinity. *J. Acoust. Soc. Am.* **110**, 1822–1827.

Shaw, S. J., Schiffers, W. P., Gentry, T. P. & Emmony, D. C. 2000 The interaction of a laser-generated cavity with a solid boundary. *J. Acoust. Soc. Am.* **107**, 3065–3071.

Tomita, Y. & Shima, A. 1986 Mechanisms of impulsive pressure generation and damage pit formation by bubble collapse. *J. Fluid Mech.* **169**, 535–564.

Tomita, Y. & Shima, A. 1990 High-speed photographic observations of laser-induced cavitation bubbles in water. *Acustica* **71**, 161–171.

Tong, R. P., Schiffers, W. P., Shaw, S. J., Blake, J. R. & Emmony, D. C. 1999 The role of 'splashing' in the collapse of a laser-generated cavity near a rigid boundary. *J. Fluid Mech.* **380**, 339–361.

Vogel, A. & Lauterborn, W. 1988 Acoustic transient generation by laser-produced cavitation bubbles near solid boundaries. *J. Acoust. Soc. Am.* **84**, 719–731.

Vogel, A., Lauterborn, W. & Timm, R. 1989 Optical and acoustic investigations of the dynamics of laser-produced cavitation bubbles near a solid boundary. *J. Fluid Mech.* **206**, 209–338.

Ward, B. & Emmony, D. C. 1991 Interferometric studies of the pressure developed in a liquid during infrared-laser-induced cavitation bubble oscillation. *Infrared Phys.* **32**, 489–515.

Wolfrum, B., Kurz, T., Lindau, O. & Lauterborn, W. 2001 Luminescence of transient bubbles at elevated ambient pressure. *Phys. Rev.* E **64**, 046306-5.

Zhang, S., Duncan, J. H. & Chahine, G. L. 1993 The final stage of the collapse of a cavitation bubble near a rigid wall. *J. Fluid Mech.* **257**, 147–181.